

Enhanced channel estimation for near-field IRS-aided multi-user MIMO system via deep residual network

Yan WANG¹, Yongqiang LI¹, Minghao Chen¹, Yu YAO¹, Feng SHU^{1,2*} & Jiangzhou WANG, Fellow, IEEE³

¹*School of Information and Communication Engineering, Hainan University, Haikou 570228, China;*

²*School of Electronic and Optical Engineering, Nanjing University of Science and Technology, Nanjing 210094, China;*

³*School of Engineering, University of Kent, Canterbury CT2 7NT, U.K.*

Abstract In this paper, channel estimation (CE) of intelligent reflecting surface aided near-field (NF) multi-user communication is investigated. Initially, the least square (LS) estimator and minimum mean square error (MMSE) estimator for the estimated channel are designed, and their mean square errors (MSEs) are derived. Subsequently, to fully harness the potential of deep residual networks (DRNs) in denoising, the above CE problem is reconceptualized as a denoising task, and a DRN-driven NF CE (DRN-NFCE) framework is proposed, and the Cramér-Rao lower bound (CRLB) is derived to serve as a benchmark for performance evaluation. In addition, to effectively capture and leverage these diverse channel features, a federated learning (FL) based global DRN-NFCE network, namely FL-DRN-NFCE, is constructed through collaborative training and joint optimization of single region DRN-NFCE (SR-DRN-NFCE) networks in different user regions. Here, users are divided into multiple regions. Correspondingly, a user region classifier based on convolutional neural network is designed to achieve the goal of matching datasets from different user regions to the corresponding SR-DRN-NFCE network. Simulation results demonstrate that the proposed FL-DRN-NFCE framework outperforms LS, MMSE, and no residual connections in terms of MSE, and the proposed FL-DRN-NFCE method has higher CE accuracy over the SR-DRN-NFCE method.

Keywords deep residual network, channel estimation, intelligent reflecting surface, near-field communication, multi-user

1 Introduction

Intelligent reflecting surfaces (IRSs), which are divided into passive IRSs [1] and active IRSs [2], can accurately transmit the signal, thereby improving the coverage and communication efficiency of the signal [3]. However, the realization of this advantage relies on precise acquisition of channel state information (CSI) [4]. In IRS assisted wireless scenarios, the introduction of IRS increases the complexity and uncertainty of signal propagation paths [5], making traditional channel estimation (CE) methods difficult to directly apply. Consequently, how to efficiently and accurately estimate the complete CSI, including the influence of IRS, has become an urgent and challenging core task in the research field of IRS-aided wireless technology [6].

1.1 Prior Works

A diversity of new algorithms and techniques have been investigated by scholars for the CE problem of IRS-aided communication networks [7]. For example, three channel estimators were developed in [8] for uplink CE of IRS-assisted multi-user (MU) massive MISO systems. Specifically, the 1st estimator cleverly utilized the element sparsity of cascaded channels for optimization; Secondly, the 2nd estimator delved into the sparsity of the common row structure inherent in the IRS to base station (BS) channel; Finally, the 3rd estimator further integrated the sparsity of common row and column structures induced by the limited scattering environment around the user, thereby achieving more refined CE. In addition, a

* Corresponding author (email: shufeng0101@163.com)

Bayesian CE method for IRS-enabled millimeter wave (mmWave) massive MIMO networks was proposed in [9]. Numerical analysis indicated that the introduction of active sensors significantly reduced the needed training cost of the designed CE algorithm. Subsequently, a two-stage strategy was proposed in [10] for estimating the sensing and communication (SAC) channels in a self-sensing IRS aided mmWave integrated sensing and communication (ISAC) network. Experimental results verified the availability of the constructed two-stage scheme. In 2022, two novel anchor assisted CE methods were investigated in [11], and the results showed that scheme I was most suitable when the BS had a significant quantity of antennas, while scheme II was more effective otherwise. In addition to focusing on researching high-performance and low complexity CE algorithms, a productive transmission protocol for CE and beam tracking was developed in [12], which independently processed satellite as well as user in a distributed way, greatly lessening the complexity of implementation.

Technically, traditional CE methods mainly rely on signal processing techniques and statistical models, such as least square (LS) CE and minimum mean square error (MMSE) CE. These methods can estimate the channel state to a certain extent, but they are often limited by the complexity of the model and the limitations of prediction accuracy. Especially in the complex and changeable wireless environment, the prediction accuracy and adaptability of traditional methods are often difficult to compliant the realistic demand.

Recently, deep learning (DL), as one of the core branches in the domain of artificial intelligence (AI), has made extraordinary breakthroughs in two key areas, namely, image recognition and natural language processing (NLP), by virtue of its excellent ability of automatic feature extraction and complex pattern recognition. The application of DL in the area of CE is expected to break through the drawbacks of traditional approach and enhance the correctness and adaptability of CE. For instance, the authors of [13] elaborated a conditional generative adversarial network (cGAN) architecture which could effectively estimate the characteristics of cascaded channels exploiting the received signal as a conditional variable. The experimental analysis fully verified that the cGAN approach exhibited excellent robust performance in the context of IRS-assisted communication networks. Subsequently, a graph neural network (GNN)-based CE algorithm was proposed in [14], which could maintain good performance with low pilot overhead. Moreover, existing neural network-based approaches typically involve manual design of network architectures through a trial-and-error process, demanding extensive domain knowledge and human resources. Therefore, an automated method for constructing a high-performance neural network architecture for CE was designed in [15], which provided the most accurate estimation of CSI over other benchmark CE methods. Specifically, the authors of [16] explored an adaptive and robust estimator for time-varying mmWave channels, considering the use of more general arbitrarily shaped IRS, in contrast to classical regular IRS elements arranged on a grid. In order to reduce complexity, a DL-based solver using fixed-point iteration and a cascaded DL network framework was studied. The proposed DL-based method exhibits lower complexity when compared to the alternating optimization (AO)-based approach, making it suitable for highly dynamic communication scenarios.

However, most of the above CE approaches are based on assumptions of far-field (FF) channel models [17]. This is because traditional wireless communication networks, i.e., the first generation (1G) to the fifth generation (5G), rely heavily on spectrum below 6 GHz or even below 3 GHz. Due to wavelength limitations, these networks typically employ smaller antenna arrays. The combination of low-dimensional antenna arrays and lower frequencies typically limits the range of wireless near-field (NF) communications to a few meters, or even a few centimeters [18]. Therefore, the depiction of traditional wireless communication networks is commonly based on FF assumptions. The 6G network architectures are expected to introduce larger antenna aperture designs and incorporate high frequency band resources, e.g. centimeter-wave, mmWave, and even terahertz, which will considerably enhance the NF effect characteristics of the network. The fusion application of emerging manners such as IRS [19], extra large-scale MIMO (XL-MIMO), and cell-free predicts that NF scenarios will become increasingly prevalent in future wireless communication. Consequently, the traditional assumption based on FF plane waves will no longer be the dominant analytical framework, and new theoretical channel models need to be sought to adapt to this change. As a result, more and more researchers have embarked on relevant studies focusing on NF communication scenarios.

Characterization and estimation algorithms for NF sparse channels have become the focus of extensive academic attention. Specifically, the authors of [20] innovatively proposed two algorithms aimed at accurately estimating the NF uplink channel in XL-MIMO systems. These algorithms cleverly exploited the spatial non-stationary characteristics unique to XL-MIMO channels, although the implementation was

accompanied by a relatively high computational complexity. In a follow-up study, a low-complexity sequential angle-distance CE (SADCE) scheme for NF XL-MIMO networks furnished with uniform planar arrays (UPAs) was designed in [21]. Notably, the prominent energy leakage effect in NF XL-MIMO channels constituted one of the key factors affecting the performance of CE. To cope with the difficult problem of compressed CE in XL-MIMO models, the authors of [22] innovatively proposed a triple parametric decomposition (TPD) structure. Simulation verification showed that this TPD skeleton considerably refined the system performance over the current state-of-the-art technology. In particular, an efficient model-based DL algorithm was investigated in [23] to estimate NF wireless channels for XL-MIMO communications. This algorithm constructed a sparse dictionary model based on spatial grids, which transformed the NF CE task in XL-MIMO systems into an optimization problem under the compressed sensing (CS) framework. Subsequently, the learning iterative shrinkage and thresholding algorithm (LISTA) was used to efficiently solve the CS problem.

However, the existing NF CE methods are mostly focused on XL-MIMO systems without IRS assistance, while corresponding CE methods for IRS-aided NF communication environments have also been explored and investigated in depth. A low complexity CE strategy based on the assumption of NF spherical wavefront was designed in [24]. To decrease pilot overhead and computational complexity, this strategy simplified the CE process into two stages. The first stage focused on angle domain variable estimation between the BS and users employing the hybrid beamforming structure, while the second stage further estimated the cascaded angle domain and polar domain factors of XL-IRS. However, in this NF channel model, only the line-of-sight (LoS) component was considered, while the non-line-of-sight (NLoS) component was ignored.

1.2 Our Contributions

Motivated by the above discussions, deep residual network (DRN)-based CE algorithms will be investigated for the IRS-aided MU NF communication. To the best of our knowledge, there is relatively little research on the application of DRN for CE in IRS assisted MU NF system, especially considering both direct and cascaded channels containing LoS and NLoS components. The core contributions of this paper are condensed into the following succinct summary:

1. To begin with, an IRS assisted NF MU communication system is constructed. For the NF channel model, unlike [24], which solely focused on the LoS component, the NLoS component is taken into account in this paper to offer a more holistic portrayal of the NF channel characteristics. Moreover, the CE problem for both direct and cascaded channels is concurrently investigated in this paper, in contrast to the prevalent focus solely on cascaded channel estimation in most studies. Subsequently, LS estimators for direct and cascaded channels are designed. Correspondingly, the closed-form expression for the mean square error (MSE) of the LS estimator is derived.
2. In order to effectively leverage the advantages of DRNs in denoising, we re-envisioned the CE problem in IRS-assisted NF MU communication systems as a denoising task and design a DRN-driven NF CE (DRN-NFCE) framework accordingly. To further validate the effectiveness and accuracy of the proposed DRN-NFCE algorithm, the Cramér-Rao lower bound (CRLB) is derived as a performance evaluation benchmark. Simulation results reveal that the proposed DRN-NFCE framework exhibits a lower level of MSE over the scheme without residual connections. In addition, compared with traditional methods such as LS and MMSE, the proposed DRN-NFCE network successfully reduces the pilot overhead by five-sixth by virtue of the powerful feature learning capability of DL technology. Correspondingly, a detailed analysis of the computational complexity of the proposed DRN-NFCE network is provided.
3. In view of the fact that the NF channel model is more sensitive to distance variations than the FF model, which leads to pronounced discrepancies in the user channel characteristics in different regions. To effectively capture and utilize these diverse channel features, users are initially divided into distinct regions predicated on pivotal parameters such as channel angle and distance. Subsequently, to precisely align datasets from disparate user regions with their respective single region DRN-NFCE (SR-DRN-NFCE) networks, a convolutional neural network (CNN) based user region classifier (RC) is designed. Simulation results show that the accuracy of the proposed RC approximates 95% in high SNR range. Further, the global DRN-NFCE based on federated learning (FL), i.e., FL-DRN-NFCE network, is obtained by collaboratively training the SR-DRN-NFCE

networks of different user regions in a FL manner. Simulation analysis shows that the proposed FL-DRN-NFCE surpasses the SR-DRN-NFCE in terms of CE accuracy.

1.3 Organization and Notation

The remainder of this paper is structured as follows. In Section 2, the system model of an IRS-aided MU NF communication is established. The CRLB is derived in Section 3. In Section 4, the RC, and FL-DRN-NFCE network are proposed, and the computational complexity of the above-mentioned networks is also given. The provision of simulation results and conclusions is carried out in Section 5 and Section 6, respectively.

Notations: Throughout the paper, matrices are denoted by boldface uppercase letter such as \mathbf{A} , vectors by boldface lowercase letter like \mathbf{a} , and scalars by lowercase letter, e.g., a . Moreover, $\mathbb{C}^{a \times b}$ stands for the space of $a \times b$ matrices with complex entries. The real part is represented by $\Re\{\cdot\}$, while the imaginary part is represented by $\Im\{\cdot\}$, respectively. Additionally, the sign $(\cdot)^T$ denotes the transpose operation, while $(\cdot)^H$ stands for conjugate and transpose operation. The signs $\|\cdot\|_2$ and $\|\cdot\|_F$ stand for the 2-norm and F -norm, respectively. The notation $\mathbb{E}\{\cdot\}$ denotes the expectation operation. $\hat{[\cdot]}$ represents the estimation operation. Furthermore, the identity matrix is denoted by \mathbf{I} , while the Kronecker and Hadamard product are respectively denoted by the symbols \otimes and \odot . $\text{diag}\{\mathbf{a}\}$ yields a diagonal matrix, where the primary diagonal elements are passively set to the components of \mathbf{a} . Finally, $\lfloor \cdot \rfloor$ indicates rounding down.

2 System model

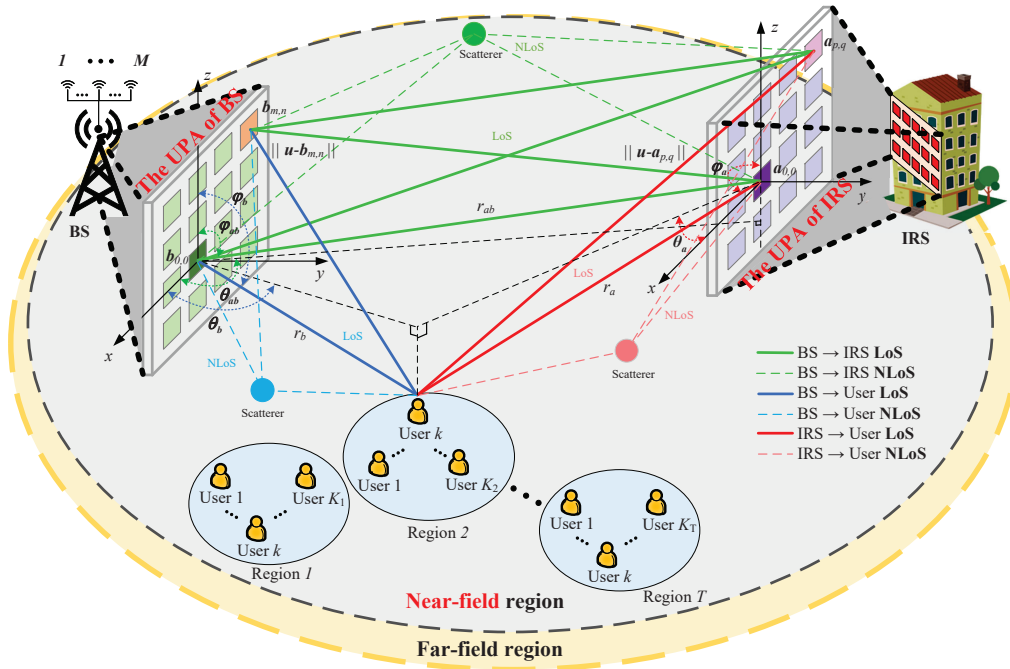


Figure 1 The system model of an IRS-aided MU MF communication.

As sketched in Fig. 1, a MU NF wireless communication system, aided by an IRS, is taken into account, with IRS being strategically positioned between the BS and single-antenna users for communication augmentation. The BS is furnished with an M -antenna array, while the IRS is composed of N reflecting elements, both of which are set up in a UPA configuration. In MU communication systems, as described in [25], a single user is often limited to information about a particular channel scenario, which leads to the possibility that neural network models trained based on the dataset collected by a single user may fail when the user crosses different regions. In order to overcome this limitation and ensure that the neural network model performs well under a wide range of channel conditions, the whole cell is elaborately

divided into T independent regions, where $t = 1, 2, \dots, T$. For the convenience of subsequent analysis, the count of users in the t -th region is explicitly defined as K_t . In particular, users in the same domain demonstrate highly similar channel characteristics, on the contrary, users distributed in distinct regions exhibit differentiated channel characteristics. Most importantly, when users migrate between regions, their channel characteristics may undergo notable changes, which puts forward higher demands for the design of neural network-based CE algorithms with high robustness.

Let $\mathbf{G} \in \mathbb{C}^{N \times M}$, $\mathbf{f}_{t,k} \in \mathbb{C}^{1 \times N}$, and $\mathbf{h}_{t,k} \in \mathbb{C}^{1 \times M}$ stand for the channels from BS to IRS, IRS to the k -th user in the t -th region, and BS to the k -th user in the t -th region, respectively, where $k = 1, 2, \dots, K_t$. The received signal at the k -th user positioned in the t -th region can be modeled as follows

$$y_{t,k} = \mathbf{h}_{t,k} \mathbf{v} x + \mathbf{f}_{t,k} \mathbf{\Theta} \mathbf{G} \mathbf{v} x + w_{t,k}, \quad (1)$$

where x represents the transmitted signal originating from the BS, and $\mathbf{v} \in \mathbb{C}^{M \times 1}$ denotes the transmit beamforming vector at BS. In addition, $\mathbf{\Theta} = \text{diag}\{\tilde{\boldsymbol{\theta}}\} \in \mathbb{C}^{N \times N}$ stands for the reflection coefficient matrix of the IRS, and $\tilde{\boldsymbol{\theta}} \in \mathbb{C}^{1 \times N}$. Moreover, $w_{t,k}$ is the AWGN at the corresponding user with $w_{t,k} \sim \mathcal{CN}(0, \sigma_w^2)$.

Since $\mathbf{f}_{t,k} \mathbf{\Theta} = \tilde{\boldsymbol{\theta}} \text{diag}\{\mathbf{f}_{t,k}\}$, it can be intuitively deduced that $\mathbf{f}_{t,k} \mathbf{\Theta} \mathbf{G} = \tilde{\boldsymbol{\theta}} \text{diag}\{\mathbf{f}_{t,k}\} \mathbf{G}$. Consequently, the core task of CE is to accurately estimate the following

$$\mathbf{H}_{t,k} = \begin{bmatrix} \mathbf{h}_{t,k} \\ \text{diag}\{\mathbf{f}_{t,k}\} \mathbf{G} \end{bmatrix} \in \mathbb{C}^{(N+1) \times M}, \quad \forall t, k. \quad (2)$$

Correspondingly, (1) can be transformed into another form of expression as follows

$$y_{t,k} = \boldsymbol{\theta} \mathbf{H}_{t,k} \mathbf{v} x + w_{t,k}, \quad (3)$$

where

$$\boldsymbol{\theta} = [1 \quad \tilde{\boldsymbol{\theta}}] \in \mathbb{C}^{1 \times (N+1)}. \quad (4)$$

2.1 Channel models

2.1.1 Near-field channel model

Drawing inspiration from [26], it is assumed that the M antennas of BS's UPA are arranged in an array of $M_{xb} \times M_{zb}$ on the $x-z$ plane, namely $M = M_{xb} \times M_{zb}$, where $M_{xb} = 2\tilde{M}_{xb} + 1$ and $M_{zb} = 2\tilde{M}_{zb} + 1$, and the antenna spacing of this array is set to d_{xb} and d_{zb} in the two dimensions, respectively. Additionally, θ_b and ϕ_b signify the azimuth angle and elevation angle of the user relative to the $x-z$ plane of BS, respectively. Also, the distance between the user and the central of BS's UPA can be represented as r_b . As a result, the coordinates of the k -th user situated in the t -th region can be given as

$$\mathbf{u}_b = (r_b \cos \theta_b \sin \phi_b, r_b \sin \theta_b \sin \phi_b, r_b \cos \phi_b). \quad (5)$$

Similarly, the coordinates of the (m, n) -th antenna of the BS's UPA are obtained as follows

$$\mathbf{b}_{m,n} = (nd_{xb}, 0, md_{zb}), \quad (6)$$

where $\forall n \in \{-\tilde{M}_{xb}, \dots, \tilde{M}_{xb}\}$, and $\forall m \in \{-\tilde{M}_{zb}, \dots, \tilde{M}_{zb}\}$.

According to [26], assuming $d_{xb}/r_b \ll 1$ and $d_{zb}/r_b \ll 1$, we can derive the propagation distance $\|\mathbf{u}_b - \mathbf{b}_{m,n}\|$ as follows

$$\begin{aligned} \|\mathbf{u}_b - \mathbf{b}_{m,n}\| &= \sqrt{(r_b \cos \theta_b \sin \phi_b - nd_{xb})^2 + (r_b \sin \theta_b \sin \phi_b)^2 + (r_b \cos \phi_b - md_{zb})^2} \\ &= r_b \sqrt{1 + \frac{n^2 d_{xb}^2}{r_b^2} + \frac{m^2 d_{zb}^2}{r_b^2} - \frac{2r_b n d_{xb} \cos \theta_b \sin \phi_b}{r_b^2} - \frac{2r_b m d_{zb} \cos \phi_b}{r_b^2}}. \end{aligned} \quad (7)$$

Subsequently, by applying the following second-order Taylor expansion to (7)

$$\sqrt{1+x} \approx 1 + \frac{1}{2}x - \frac{1}{8}x^2 + \mathcal{O}(x^2), \quad (8)$$

then, (7) can be approximated as

$$\|\mathbf{u}_b - \mathbf{b}_{m,n}\| \approx \underbrace{r_b - nd_{xb} \cos \theta_b \sin \phi_b + \frac{n^2 d_{xb}^2 (1 - \cos^2 \theta_b \sin^2 \phi_b)}{2r_b}}_{h_1, \text{ only depend on } n} - \underbrace{md_{zb} \cos \phi_b + \frac{m^2 d_{zb}^2 \sin^2 \phi_b}{2r_b}}_{h_2, \text{ only depend on } m}, \quad (9)$$

where h_1 and h_2 solely contingent on n and m , respectively.

Referring to the uniform spherical wave (USW) model of [27], [28], the NF LoS MISO channel can be formulated as follows

$$\mathbf{h}_{t,k}^{\text{LoS}} = \beta_b e^{-j \frac{2\pi}{\lambda} r_b} \left[e^{-j \frac{2\pi}{\lambda} \left(\|\mathbf{u}_b - \mathbf{b}_{-\tilde{M}_{xb}, -\tilde{M}_{zb}}\| - r_b \right)}, \dots, e^{-j \frac{2\pi}{\lambda} \left(\|\mathbf{u}_b - \mathbf{b}_{\tilde{M}_{xb}, \tilde{M}_{zb}}\| - r_b \right)} \right]^T, \quad (10)$$

Once the constant phase $e^{-j \frac{2\pi}{\lambda} r_b}$ is taken out, the resulting phase of the Array Response Vector (ARV) is obtained, referred to as h_1 and h_2 . More specifically, the ARV of BS-user channel is as follows

$$\mathbf{a}(\theta_b, \phi_b, r_b) = \mathbf{a}_x(\theta_b, \phi_b, r_b) \otimes \mathbf{a}_z(\phi_b, r_b), \quad (11)$$

where

$$[\mathbf{a}_x(\theta_b, \phi_b, r_b)]_n = e^{-j \frac{2\pi}{\lambda} \cdot h_1} = e^{-j \frac{2\pi}{\lambda} \left(-n d_{xb} \cos \theta_b \sin \phi_b + \frac{n^2 d_{xb}^2 (1 - \cos^2 \theta_b \sin^2 \phi_b)}{2r_b} \right)}, \quad (12)$$

and

$$[\mathbf{a}_z(\phi_b, r_b)]_m = e^{-j \frac{2\pi}{\lambda} \cdot h_2} = e^{-j \frac{2\pi}{\lambda} \left(-m d_{zb} \cos \phi_b + \frac{m^2 d_{zb}^2 \sin^2 \phi_b}{2r_b} \right)}. \quad (13)$$

As demonstrated in Fig. 1, the multipath effect in NF environment, originating from the refraction and reflection of signals triggered by scatterers, prompts the signals to reach the users via NLoS paths, and this stochasticity endows the channel with dynamic characteristics, which urgently requires a statistical model to capture its changing patterns. In this context, the channel from BS to scatterer can be analogized to the MISO channel model, and thus, a novel expression of NF multipath channel can be constructed as follows

$$\mathbf{h}_{t,k} = \underbrace{\beta_b \mathbf{a}(\theta_b, \phi_b, r_b)}_{\text{LoS}} + \sum_{\ell=1}^{L_b} \underbrace{\tilde{\beta}_{b,\ell} \mathbf{a}(\tilde{\theta}_{b,\ell}, \tilde{\phi}_{b,\ell}, \tilde{r}_{b,\ell})}_{\text{NLoS}}. \quad (14)$$

where L_b denotes the number of scatterers between the BS and the user, and $\ell = 1, 2, \dots, L_b$. Moreover, $\tilde{\theta}_{b,\ell}$, $\tilde{\phi}_{b,\ell}$, $\tilde{r}_{b,\ell}$, and $\tilde{\beta}_{b,\ell}$ represent the corresponding azimuth, elevation, distance, and channel gain of the ℓ -th scatterer, respectively.

Likewise, the UPA of IRS is also placed in the $x - z$ plane, parallel to BS's UPA. For the k -th user positioned in the t -th region, their coordinates relative to IRS's UPA are articulated by

$$\mathbf{u}_a = (r_a \cos \theta_a \sin \phi_a, r_a \sin \theta_a \sin \phi_a, r_a \cos \phi_a), \quad (15)$$

where θ_a , ϕ_a , and r_a are the user's azimuth angle and elevation angle with respect to the IRS, respectively, and the user's distance from the IRS center element. Correspondingly, the (p, q) -th element of the IRS's element array are given by

$$\mathbf{a}_{p,q} = (q d_{xa}, 0, p d_{za}), \quad \forall q \in \{-\tilde{N}_{xa}, \dots, \tilde{N}_{xa}\}, \quad p \in \{-\tilde{N}_{za}, \dots, \tilde{N}_{za}\}, \quad (16)$$

where $N = N_{xa} \times N_{za}$, and $N_{xa} = 2\tilde{N}_{xa} + 1$ and $N_{za} = 2\tilde{N}_{za} + 1$. Correspondingly, the element spacing of IRS's UPA along the x and z axis is represented by d_{xa} and d_{za} , respectively.

Similar to (7), by employing (8), the distance between the k -th user in the t -th region and the (p, q) -th element of the IRS is as follows

$$\|\mathbf{u}_a - \mathbf{a}_{p,q}\| \approx \underbrace{r_a - q d_{xa} \cos \theta_a \sin \phi_a + \frac{q^2 d_{xa}^2 (1 - \cos^2 \theta_a \sin^2 \phi_a)}{2r_a}}_{f_1, \text{ only depend on } q} - \underbrace{p d_{za} \cos \phi_a + \frac{p^2 d_{za}^2 \sin^2 \phi_a}{2r_a}}_{f_2, \text{ only depend on } p}, \quad (17)$$

thus, referring to [26], the ARV of IRS-user channel can be displayed as follows

$$\mathbf{a}(\theta_a, \phi_a, r_a) = \mathbf{a}_x(\theta_a, \phi_a, r_a) \otimes \mathbf{a}_z(\phi_a, r_a), \quad (18)$$

where

$$[\mathbf{a}_x(\theta_a, \phi_a, r_a)]_q = e^{-j \frac{2\pi}{\lambda} \cdot f_1} = e^{-j \frac{2\pi}{\lambda} \left(-q d_{xa} \cos \theta_a \sin \phi_a + \frac{q^2 d_{xa}^2 (1 - \cos^2 \theta_a \sin^2 \phi_a)}{2r_a} \right)}, \quad (19)$$

and

$$[\mathbf{a}_z(\phi_a, r_a)]_p = e^{-j \frac{2\pi}{\lambda} \cdot f_2} = e^{-j \frac{2\pi}{\lambda} \left(-p d_{za} \cos \phi_a + \frac{p^2 d_{za}^2 \sin^2 \phi_a}{2r_a} \right)}. \quad (20)$$

As depicted in Fig. 1, the presence of scatterers within the environment can elicit multipath effects in the IRS-user NF channel. Hence, the channel between the k -th user in the t -th region and the IRS can be formulated as

$$\mathbf{f}_{t,k} = \underbrace{\beta_a \mathbf{a}(\theta_a, \phi_a, r_a)}_{\text{LoS}} + \sum_{\ell=1}^{L_a} \underbrace{\tilde{\beta}_{a,\ell} \mathbf{a}(\tilde{\theta}_{a,\ell}, \tilde{\phi}_{a,\ell}, \tilde{r}_{a,\ell})}_{\text{NLoS}}, \quad (21)$$

where L_a is the count of scatterers between IRS and user, and the azimuth angle, elevation angle, and distance of the ℓ -th scatterer are represented as $\tilde{\theta}_{a,\ell}$, $\tilde{\phi}_{a,\ell}$, and $\tilde{r}_{a,\ell}$.

As can be illustrated in Fig. 1, the NLoS MIMO path can be conceptualized as the fusion of two distinct MISO channels with respect to the BS and IRS, respectively. As a result, the channel between BS and IRS can be written as follows

$$\mathbf{G} = \mathbf{G}_{\text{LoS}} + \sum_{\ell=1}^{L_{ba}} \underbrace{\tilde{\beta}_{\ell} \mathbf{a}(\tilde{\theta}_{ba,\ell}, \tilde{\phi}_{ba,\ell}, \tilde{r}_{ba,\ell}) \mathbf{a}^T(\tilde{\theta}_{ab,\ell}, \tilde{\phi}_{ab,\ell}, \tilde{r}_{ab,\ell})}_{\text{NLoS}}, \quad (22)$$

where the quantity of scatterers is designated as L_{ba} . In addition, $\tilde{\theta}_{ba,\ell}$ ($\tilde{\theta}_{ab,\ell}$) is the azimuth angle of the ℓ -th scatterer with respect to the $x-z$ plane of IRS (BS), and the elevation angle of the ℓ -th scatterer with respect to the $x-z$ plane of IRS (BS) is signified as $\tilde{\phi}_{ba,\ell}$ ($\tilde{\phi}_{ab,\ell}$). In particular, $\tilde{r}_{ba,\ell}$ ($\tilde{r}_{ab,\ell}$) denotes the distance between the ℓ -th scatterer and the central element of IRS (BS). More precisely, according to [26], \mathbf{G}_{LoS} can be embodied as follows

$$\mathbf{G}_{\text{LoS}} = \tilde{\beta} \mathbf{a}(\theta_{ba}, \phi_{ba}, r_{ba}) \left(\mathbf{a}(\theta_{ab}, \phi_{ab}, r_{ab}) \right)^T \odot (\mathbf{G}_c^x \otimes \mathbf{G}_c^z), \quad (23)$$

where

$$[\mathbf{G}_c^x]_{q,n} = e^{-j \frac{2\pi}{\lambda r_{ab}} n d_{xb} q d_{xa} (1 - \cos^2 \theta_{ab} \sin^2 \phi_{ab})}, \quad (24)$$

and

$$[\mathbf{G}_c^z]_{p,m} = e^{-j \frac{2\pi}{\lambda r_{ab}} m d_{zb} p d_{za} \sin^2 \phi_{ab}}. \quad (25)$$

In (23), (24), and (25), θ_{ba} (θ_{ab}) and ϕ_{ba} (ϕ_{ab}) represent the azimuth and elevation angles of the center of BS (IRS) relative to the center of IRS (BS), respectively. Besides, $r_{ba} = r_{ab} = \|\mathbf{a}_{0,0} - \mathbf{b}_{0,0}\|$ denote the distance between the central of IRS and the central of BS. As evident from (23), the NF LoS MIMO path matrix between parallel UPAs incorporates a interleaved variable, namely $\mathbf{G}_c^x \otimes \mathbf{G}_c^z$, which cannot be simply decomposed into the direct product of the ARVs of BS-side and IRS-side.

2.1.2 Far-field channel model

As a comparison, the FF ARV can be specifically described as follows

$$\begin{aligned} \mathbf{a}_{\text{far}}(\theta_b, \phi_b) &= \left[e^{-j \frac{2\pi}{\lambda} \tilde{M}_{xb} d_{xb} \cos \theta_b \sin \phi_b}, \dots, e^{j \frac{2\pi}{\lambda} \tilde{M}_{xb} d_{xb} \cos \theta_b \sin \phi_b} \right]^T \\ &\otimes \left[e^{-j \frac{2\pi}{\lambda} \tilde{M}_{zb} d_{zb} \cos \phi_b}, \dots, e^{j \frac{2\pi}{\lambda} \tilde{M}_{zb} d_{zb} \cos \phi_b} \right]^T. \end{aligned} \quad (26)$$

Correspondingly, in this case, according to [26], the FF channel model between BS-user, IRS-user, and BS-IRS can be modeled as follows

$$\mathbf{h}_{t,k}^{\text{far}} = \underbrace{\beta_b \mathbf{a}_{\text{far}}(\theta_b, \phi_b)}_{\text{LoS}} + \sum_{\ell=1}^{L_b} \underbrace{\tilde{\beta}_{b,\ell} \mathbf{a}_{\text{far}}(\tilde{\theta}_{b,\ell}, \tilde{\phi}_{b,\ell})}_{\text{NLoS}}, \quad (27)$$

$$\mathbf{f}_{t,k}^{\text{far}} = \underbrace{\beta_a \mathbf{a}_{\text{far}}(\theta_a, \phi_a)}_{\text{LoS}} + \sum_{\ell=1}^{L_a} \underbrace{\tilde{\beta}_{a,\ell} \mathbf{a}_{\text{far}}(\tilde{\theta}_{a,\ell}, \tilde{\phi}_{a,\ell})}_{\text{NLoS}}, \quad (28)$$

and

$$\mathbf{G}^{\text{far}} = \mathbf{G}_{\text{LoS}}^{\text{far}} + \sum_{\ell=1}^{L_{ba}} \underbrace{\tilde{\beta}_{\ell} \mathbf{a}_{\text{far}}(\tilde{\theta}_{ba,\ell}, \tilde{\phi}_{ba,\ell}) \mathbf{a}_{\text{far}}^T(\tilde{\theta}_{ab,\ell}, \tilde{\phi}_{ab,\ell})}_{\text{NLoS}}, \quad (29)$$

in which, in the FF scenario, the LoS component between the BS and IRS channels can be expressed as

$$\mathbf{G}_{\text{LoS}}^{\text{far}} = \tilde{\beta} \mathbf{a}_{\text{far}}(\theta_{ba}, \phi_{ba}) \left(\mathbf{a}_{\text{far}}(\theta_{ab}, \phi_{ab}) \right)^T. \quad (30)$$

2.2 Problem formulation

To ascertain the downlink direct and cascaded channel, i.e. $\mathbf{H}_{t,k}$, BS transmits predetermined pilot signals to users, facilitated by the IRS, spanning across Q time slots, where $q = 1, 2, \dots, Q$. Drawing upon (3), $y_{t,k,q}^p$ for the k -th user in the t -th region, in the q -th time slot, is mathematically formulated as follows

$$y_{t,k,q}^p = \boldsymbol{\theta}_q \mathbf{H}_{t,k} \mathbf{v} p_q + w_{t,k,q}, \quad (31)$$

where the pilot signal transmitted by BS is signified as p_q , and $\boldsymbol{\theta}_q$ stands for the IRS phase shift within the current time slot. Also, $w_{t,k,q}$ denotes the noise at the user of the current time slot.

Following the transmission of pilot signals across Q consecutive time slots, we derive the comprehensive $Q \times 1$ received pilot vector as depicted below.

$$\mathbf{y}_{t,k}^p = [y_{t,k,1}^p, y_{t,k,2}^p, \dots, y_{t,k,Q}^p]^T = \boldsymbol{\Phi} \mathbf{H}_{t,k} \mathbf{v} p_{t,k,q} + \mathbf{w}_{t,k}, \quad (32)$$

where $\boldsymbol{\Phi} = [\boldsymbol{\theta}_1^T, \boldsymbol{\theta}_2^T, \dots, \boldsymbol{\theta}_Q^T]^T \in \mathbb{C}^{Q \times (N+1)}$ and $\mathbf{w}_{t,k} = [w_{t,k,1}, w_{t,k,2}, \dots, w_{t,k,Q}]^T \in \mathbb{C}^{Q \times 1}$. According to [25], assuming $p_{t,k,q} = 1$ for the purpose of subsequent CE, (32) can be rephrased as

$$\mathbf{y}_{t,k}^p = \boldsymbol{\Phi} \mathbf{H}_{t,k} \mathbf{v} + \mathbf{w}_{t,k}. \quad (33)$$

Due to the fact that $\text{vec}(\mathbf{ABC}) = (\mathbf{C}^T \otimes \mathbf{A}) \text{vec}(\mathbf{B})$, (33) can be reformulated as

$$\mathbf{y}_{t,k}^p = \underbrace{(\mathbf{v}^T \otimes \boldsymbol{\Phi})}_{\mathbf{A}_{t,k}} \underbrace{\text{vec}(\mathbf{H}_{t,k})}_{\mathbf{h}'_{t,k}} + \mathbf{w}_{t,k} = \mathbf{A}_{t,k} \mathbf{h}'_{t,k} + \mathbf{w}_{t,k}. \quad (34)$$

It follows from (34) that the essence of CE lies in reconstructing $\mathbf{h}'_{t,k}$ utilizing the known $\mathbf{y}_{t,k}^p$ and $\mathbf{A}_{t,k}$. According to [29], the estimated $\mathbf{h}'_{t,k}$ using LS estimator is provided by

$$\hat{\mathbf{h}}'_{t,k,\text{LS}} = \mathbf{A}_{t,k}^\dagger \mathbf{y}_{t,k}^p, \quad (35)$$

where $\mathbf{A}_{t,k}^\dagger = \mathbf{A}_{t,k}^H (\mathbf{A}_{t,k} \mathbf{A}_{t,k}^H)^{-1}$ denotes the pseudoinverse of $\mathbf{A}_{t,k}$.

The estimation MSE of (35) is

$$\varepsilon_{\text{LS}} = \mathbb{E}\{\|\mathbf{h}'_{t,k} - \hat{\mathbf{h}}'_{t,k,\text{LS}}\|_F^2\} = \mathbb{E}\{\|\mathbf{h}'_{t,k} - \mathbf{A}_{t,k}^\dagger (\mathbf{A}_{t,k} \mathbf{h}'_{t,k} + \mathbf{w}_{t,k})\|_F^2\} = \sigma_u^2 \text{tr}((\mathbf{A}_{t,k} \mathbf{A}_{t,k}^H)^{-H}). \quad (36)$$

It is worth noting that since $\mathbf{A}_{t,k} = \mathbf{v}^T \otimes \boldsymbol{\Phi}$, \mathbf{v} and $\boldsymbol{\Phi}$ need to be pre-determined to be constant values as a prerequisite for CE. Consequently, according to [30], the transmit beamforming vector \mathbf{v} randomly selects their components from $\{-\frac{1}{\sqrt{M}}, +\frac{1}{\sqrt{M}}\}$. Furthermore, based on [31], $\boldsymbol{\Phi}$ can be innovatively crafted as a discrete Fourier transform (DFT), namely,

$$\boldsymbol{\Phi}^T = \begin{bmatrix} 1 & 1 & \dots & 1 \\ 1 & W_Q & \dots & W_Q^{Q-1} \\ \dots & \dots & \ddots & \dots \\ 1 & W_Q^N & \dots & W_Q^{N(Q-1)} \end{bmatrix} \in \mathbb{C}^{(N+1) \times Q}, \quad (37)$$

where $W_Q = e^{j2\pi/Q}$.

Subsequently, the MMSE estimator for the channel $\mathbf{h}'_{t,k}$ is

$$\hat{\mathbf{h}}'_{t,k,\text{MMSE}} = \mathbf{W}_{\text{MMSE}} \hat{\mathbf{h}}'_{t,k,\text{LS}}. \quad (38)$$

Correspondingly, the MMSE estimator obtains an estimate based on \mathbf{W} to minimize the MSE in the following given equation

$$\varepsilon_{\text{MMSE}} = \mathbb{E}\{\|\mathbf{h}'_{t,k} - \mathbf{W}_{\text{MMSE}} \hat{\mathbf{h}}'_{t,k,\text{LS}}\|_F^2\}. \quad (39)$$

By solving the problem presented in equation (39), the following outcomes can be derived:

$$\mathbf{W}_{\text{MMSE}} = \mathbf{R}_{\mathbf{h}'_{t,k} \hat{\mathbf{h}}'_{t,k,\text{LS}}} \left(\mathbf{R}_{\hat{\mathbf{h}}'_{t,k,\text{LS}} \hat{\mathbf{h}}'_{t,k,\text{LS}}} + \frac{\sigma_u^2}{\sigma_x^2} \mathbf{I} \right)^{-1}, \quad (40)$$

where $\mathbf{R}_{\mathbf{h}'_{t,k} \hat{\mathbf{h}}'_{t,k,\text{LS}}} = \mathbb{E}\{\mathbf{h}'_{t,k} \hat{\mathbf{h}}'_{t,k,\text{LS}}^H\}$ represents the cross-correlation matrix between the actual channel and the LS CE, while $\mathbf{R}_{\hat{\mathbf{h}}'_{t,k,\text{LS}} \hat{\mathbf{h}}'_{t,k,\text{LS}}} = \mathbb{E}\{\hat{\mathbf{h}}'_{t,k,\text{LS}} \hat{\mathbf{h}}'_{t,k,\text{LS}}^H\}$ denotes the autocorrelation matrix of the LS CE.

3 CRLB

The CRLB is often used to calculate the optimal estimation accuracy that can be achieved theoretically, which can evaluate the effectiveness of proposed CE algorithms. For the CE problem (34), $\mathbf{A}_{t,k}$ is a real matrix, $\mathbf{y}_{t,k}^p \in \mathbb{C}^{Q \times 1}$ represents the known received signal, $\mathbf{h}'_{t,k}$ denotes the channel to be estimated, and $\mathbf{w}_{t,k}$ is the whitened noise. Consequently, (34) can be divided into two parts, where the real part is

$$\mathbf{y}_{t,k,u}^p = \mathbf{A}_{t,k} \mathbf{h}'_{t,k,u} + \mathbf{w}_{t,k,u}, \quad (41)$$

and the imaginary part is as follows

$$\mathbf{y}_{t,k,v}^p = \mathbf{A}_{t,k} \mathbf{h}'_{t,k,v} + \mathbf{w}_{t,k,v}, \quad (42)$$

where

$$\begin{aligned} \mathbf{y}_{t,k,u}^p &= \Re\{\mathbf{y}_{t,k}^p\}, \quad \mathbf{y}_{t,k,v}^p = \Im\{\mathbf{y}_{t,k}^p\}, \\ \mathbf{h}'_{t,k,u} &= \Re\{\mathbf{h}'_{t,k}\}, \quad \mathbf{h}'_{t,k,v} = \Im\{\mathbf{h}'_{t,k}\}, \\ \mathbf{w}_{t,k,u} &= \Re\{\mathbf{w}_{t,k}\}, \quad \mathbf{w}_{t,k,v} = \Im\{\mathbf{w}_{t,k}\}. \end{aligned} \quad (43)$$

Thus, the CRLB of $\hat{\mathbf{h}}'_{t,k}$ can also be divided into two parts, which are shown as

$$\gamma_{t,k} = \gamma_{t,k}^u + \gamma_{t,k}^v = \mathbb{E} \left\{ \left\| \hat{\mathbf{h}}'_{t,k,u} - \mathbf{h}'_{t,k,u} \right\|^2 \right\} + \mathbb{E} \left\{ \left\| \hat{\mathbf{h}}'_{t,k,v} - \mathbf{h}'_{t,k,v} \right\|^2 \right\}. \quad (44)$$

In this case, we first consider real part (41). Since the $\mathbf{w}_{t,k,u}$ follows the distribution of Gaussian distribution with 0 mean and σ_u^2 variance, the conditional probability density function of $\mathbf{y}_{t,k,u}^p$ with the given $\mathbf{h}'_{t,k,u}$ is

$$p_{\mathbf{y}_{t,k,u}^p | \mathbf{h}'_{t,k,u}}(\mathbf{y}_{t,k,u}^p; \mathbf{h}'_{t,k,u}) = \frac{1}{(2\pi\sigma_u^2)^{Q/2}} \exp \left\{ -\frac{1}{2\sigma_u^2} \left\| \mathbf{y}_{t,k,u}^p - \mathbf{A}_{t,k} \mathbf{h}'_{t,k,u} \right\|^2 \right\}. \quad (45)$$

The Fisher information matrix of (41) can then be derived as

$$[\mathbf{J}]_{i,j} = -\mathbb{E} \left\{ \frac{\partial \mathbf{y}_{t,k,u}^p | \mathbf{h}'_{t,k,u}}{\partial h'_{t,k,u,i}} \frac{\partial \mathbf{y}_{t,k,u}^p | \mathbf{h}'_{t,k,u}}{\partial h'_{t,k,u,j}} \right\} = \frac{1}{\sigma_u^2} [\mathbf{A}_{t,k}^H \mathbf{A}_{t,k}]_{i,j}, \quad (46)$$

where $h'_{t,k,u,i}$, $h'_{t,k,u,j}$ denote the i -th and j -th entry of $\mathbf{h}'_{t,k,u}$. Then, the real part $\gamma_{t,k}^u$ is

$$\gamma_{t,k}^u = \mathbb{E} \left\{ \left\| \hat{\mathbf{h}}'_{t,k,u} - \mathbf{h}'_{t,k,u} \right\|^2 \right\} \geq \text{Tr} \{ \mathbf{J}_u^{-1} \} = \sigma_u^2 \text{Tr} \{ (\mathbf{A}_{t,k}^H \mathbf{A}_{t,k})^{-1} \}. \quad (47)$$

Since $\mathbf{A}_{t,k} = \mathbf{v}^T \otimes \Phi$, $(\mathbf{A}_{t,k}^H \mathbf{A}_{t,k})^{-1}$ can be presented as

$$(\mathbf{A}_{t,k}^H \mathbf{A}_{t,k})^{-1} = \left((\mathbf{v}^T \otimes \Phi)^H (\mathbf{v}^T \otimes \Phi) \right)^{-1} = \left((\mathbf{v}\mathbf{v}^H)^{-1} \right)^T \otimes (\Phi^H \Phi)^{-1}. \quad (48)$$

Since $\text{tr}(\mathbf{A} \otimes \mathbf{B}) = \text{tr}(\mathbf{A})\text{tr}(\mathbf{B})$ and $\text{tr}(\mathbf{A}^T) = \text{tr}(\mathbf{A})$, thus, $\text{tr} \{ (\mathbf{A}_{t,k}^H \mathbf{A}_{t,k})^{-1} \}$ can be calculated as

$$\text{tr} \{ (\mathbf{A}_{t,k}^H \mathbf{A}_{t,k})^{-1} \} = \text{tr} \left(\left((\mathbf{v}\mathbf{v}^H)^{-1} \right)^T \right) \text{tr} \left((\Phi^H \Phi)^{-1} \right) = \text{tr} \left((\mathbf{v}\mathbf{v}^H)^{-1} \right) \text{tr} \left((\Phi^H \Phi)^{-1} \right). \quad (49)$$

Assuming $\{\alpha_i\}_{i=1}^M$ is denoted as the M eigenvalues of the matrix of $\mathbf{v}\mathbf{v}^H$, and $\{\beta_j\}_{j=1}^{N+1}$ is denoted as the $N+1$ eigenvalues of the matrix of $\Phi^H \Phi$, then

$$\text{tr} \{ (\mathbf{A}_{t,k}^H \mathbf{A}_{t,k})^{-1} \} = \left(\sum_{i=1}^M \alpha_i^{-1} \right) \left(\sum_{j=1}^{N+1} \beta_j^{-1} \right). \quad (50)$$

According to [32], we have

$$\text{tr} \{ (\mathbf{A}_{t,k}^H \mathbf{A}_{t,k})^{-1} \} \geq M \left(M / \sum_{i=1}^M \alpha_i \right) (N+1) \left((N+1) / \sum_{j=1}^{N+1} \beta_j \right) = \frac{M^2 (N+1)^2}{\text{tr}(\mathbf{v}\mathbf{v}^H) \text{tr}(\Phi^H \Phi)}. \quad (51)$$

Finally, the CRLB of the real part of $\hat{\mathbf{h}}'_{t,k}$ becomes

$$\gamma_{t,k}^u = \mathbb{E} \left\{ \left\| \hat{\mathbf{h}}'_{t,k,u} - \mathbf{h}'_{t,k,u} \right\|^2 \right\} = \sigma_u^2 \frac{M(N+1)}{Q}. \quad (52)$$

Observing equations (41) and (42), it can be seen that the real part and imaginary part have the same form, namely

$$\gamma_{t,k}^v = \gamma_{t,k}^u = \sigma_u^2 \frac{M(N+1)}{Q}. \quad (53)$$

Thus, the CRLB of (34) is as follows

$$\gamma_{t,k} = \gamma_{t,k}^u + \gamma_{t,k}^v = 2\sigma_u^2 \frac{M(N+1)}{Q}. \quad (54)$$

4 Proposed FL-DRN-NFCE algorithm

4.1 The basic principle of the proposed DRN-NFCE algorithm

Specifically, the proposed DRN-NFCE network introduces a non-linear function \mathbf{f}_θ between $\mathbf{y}_{t,k}^p$ and $\widehat{\mathbf{h}}'_{t,k,\text{DRN}}$, which can be mathematically expressed as

$$\widehat{\mathbf{h}}'_{t,k,\text{DRN}} = \mathbf{f}_\theta(\mathbf{y}_{t,k}^p), \quad (55)$$

where θ represents weight. Accordingly, the expression for the loss function is as follows

$$\mathcal{L}(\theta) = \frac{1}{S_{t,k}} \sum_{s=1}^{S_{t,k}} \|\widehat{\mathbf{h}}'_{t,k,\text{DRN}} - \widehat{\mathbf{h}}'_{t,k,\text{LS}}\|_2^2, \quad (56)$$

where $S_{t,k}$ stands for the size of training dataset. The traditional LS CE scheme can be used to obtain the label $\widehat{\mathbf{h}}'_{t,k,\text{LS}}$. The objective of exploiting the proposed DRN-NFCE network for CE is to minimize $\mathcal{L}(\theta)$ by optimizing θ , which is

$$\min_{\theta} \mathcal{L}(\theta) = \frac{1}{S_{t,k}} \sum_{s=1}^{S_{t,k}} \|\mathbf{f}_\theta(\mathbf{y}_{t,k}^p) - \widehat{\mathbf{h}}'_{t,k,\text{LS}}\|_2^2. \quad (57)$$

In each iteration i , θ are updated through the following way, namely,

$$\theta_{i+1} = \theta_i - \lambda_i \mathbf{g}(\theta_i), \quad (58)$$

where $\mathbf{g}(\theta_i)$ is the gradient vector (GV) for θ_i , and λ_i is the learning rate (LR).

4.2 The proposed FL-DRN-NFCE neural network

As diagrammed in Fig. 1, considering that the NF model is more sensitive to changes in distance, angle, and other factors than the FF model, which results in significant differences in the channel characteristics of users in different regions. In order to effectively capture and fully utilize these diverse channel characteristics, the entire region is divided into T different sub regions. Therefore, in order to accurately match datasets from different user regions with corresponding SR-DRN-NFCE networks, a CNN-based RC is firstly designed.

Table 1 Hyperparameters of the proposed RC network.

Layers	Operations	Number of parameters
1	Conv+BN+ReLU	$(3 \times 3 \times 2) \times 32$
2	Conv+BN+ReLU	$(3 \times 3 \times 32) \times 64$
3	Conv+BN+ReLU	$(3 \times 3 \times 64) \times 128$
4	Conv	$(1 \times 1 \times 128) \times 2$
5	Linear	$(Q \times 1 \times 2) \times (3 \times 1 \times 1) + (3 \times 1 \times 1)$

As shown in Table 1, the proposed RC network architecture comprises four convolution (Conv) layers and a linear layer. To enhance the steadiness of the model and expedite the training efficiency, a batch normalization (BN) is introduced between Conv and the rectified linear unit (ReLU). The first three layers are all ‘‘Conv + BN + ReLU’’ operations, where the Conv layer is responsible for extracting features from the input signal. Importantly, the count of channels in these layers progressively increases from the first to the third. Specifically, the input of the proposed RC network is the received pilot signal $\mathbf{y}_{t,k}^p$, which includes both real and imaginary parts, therefore, the initial number of channels is 2. Upon passing through the first Conv layer, the channel number increases to 32, enabling the network to capture a broader range of features. After the second Conv layer, the channel number escalates further to 64, enhancing the network’s capacity to represent complex signal patterns. Finally, after the third Conv layer, the channel number reaches 128, significantly boosting the network’s discriminative power and enabling it to better differentiate between similar signals, particularly in regions where signals may overlap or exhibit similar characteristics - this is crucial for capturing intricate patterns and subtle differences within the signal. BN is employed to enhance training stability and accelerate convergence, while the ReLU activation function introduces nonlinearity, thereby bolstering the network’s expressive capacity. The fourth layer specifically utilizes a 1×1 Conv kernel for dimensionality reduction of the feature maps

received from the preceding layer, reducing the channel number back to 2. This step effectively reduces the parameters and computational complexity of the subsequent linear layer. The entire network is meticulously designed to efficiently extract signal features while mitigating computational load through dimensionality reduction. Ultimately, the linear layer maps the signals to category labels, achieving precise and efficient region classification of signals.

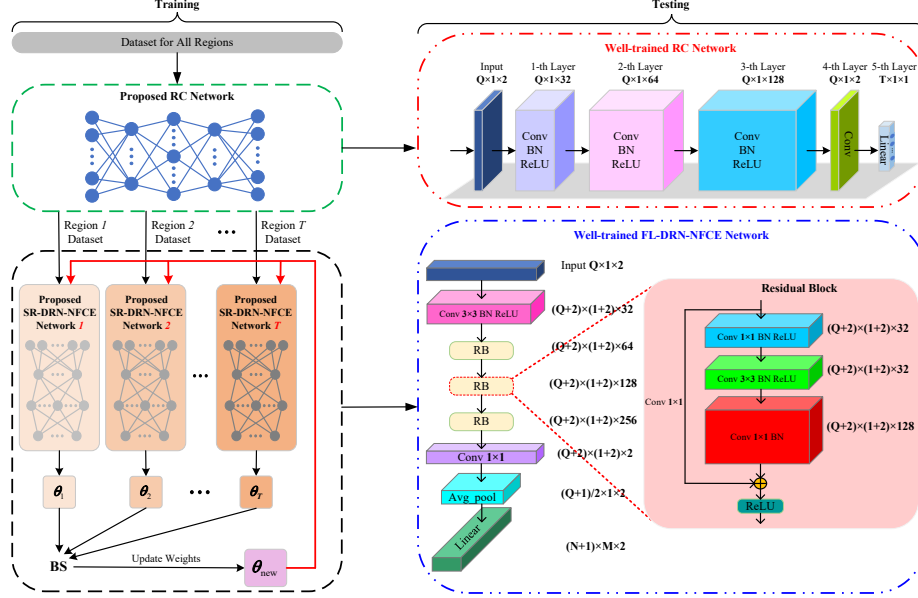


Figure 2 The proposed FL-DRN-NFCE network.

Subsequently, as shown in Fig. 2, the user datasets of all regions are input into the well-trained RC network, then, users in each region calculate local GVs based on the current region's dataset. Once the BS has collected the local GVs of all regions, collaborative training is performed between the BS and the user in a FL manner, i.e., the BS updates the weights via the following manner

$$\theta_{i+1} = \theta_i - \lambda_i \frac{1}{\sum_{t=1}^T K_t} \sum_{t=1}^T \sum_{k=1}^{K_t} \mathbf{g}_{t,k}(\theta_i). \quad (59)$$

Finally, the well-trained FL-DRN-NFCE network is obtained in Fig. 2.

Table 2 Hyperparameters of the proposed FL-DRN-NFCE network.

Input		
The received pilot signal $\mathbf{y}_{t,k}^p$ with the size of $Q \times 1$		
Layers	Operations	Number of parameters
1	Conv+BN+ReLU	$(3 \times 3 \times 2) \times 32$
2	RB	$(1 \times 1 \times 32) \times 16 + (3 \times 3 \times 16) \times 16 + (1 \times 1 \times 16) \times 64 + (1 \times 1 \times 32) \times 64$
3	RB	$(1 \times 1 \times 64) \times 32 + (3 \times 3 \times 32) \times 32 + (1 \times 1 \times 32) \times 128 + (1 \times 1 \times 64) \times 128$
4	RB	$(1 \times 1 \times 128) \times 64 + (3 \times 3 \times 64) \times 64 + (1 \times 1 \times 64) \times 256 + (1 \times 1 \times 128) \times 256$
5	Conv	$(1 \times 1 \times 256) \times 2$
6	Avg-pool	-
7	Linear	$(\lfloor \frac{Q+1}{2} \rfloor \times 1 \times 2) \times ((N+1) \times M \times 2) + (N+1) \times M \times 2$
Output		
The estimated channel with the size of $(N+1)M \times 1$		

Specifically, as displayed in Table 2, the proposed FL-DRN-NFCE comprises two Conv layers, one average pool (Avg-pool) layer, one linear layer, and three residual blocks (RBs). The first layer is configured as a Conv layer with padding set to 2, a kernel size of 3, and a stride of 1. This design expands the input signal's dimensions in height and width from $Q \times 1$ to $(Q+2) \times (1+2)$, aiming to meet the requirements of feature extraction in subsequent Conv layers and dimensionality reduction in

Avg-pool layers. Layers 2 to 4 consist of three consecutive RBs [33] [34], characterized by their unique approach: initially reducing the dimensionality of the feature map using a 1×1 Conv kernel, followed by a standard Conv layer for feature extraction, and finally employing another 1×1 Conv kernel to expand the count of channels in the feature map. This design strategy offers significant advantages in reducing computational load and enhancing model efficiency. Additionally, to maintain dimensional consistency in the residual connections, an extra 1×1 Conv kernel is utilized for dimensionality adjustment. The specific parameter configuration of the second RB is detailed in Fig. 2: the input feature map has dimensions of $(Q + 2) \times (1 + 2) \times 64$, and the output feature map has dimensions of $(Q + 2) \times (1 + 2) \times 128$. Within the 2nd RB, the number of channels is first reduced to 32, which halves the number of parameters in the intermediate Conv layer for feature extraction, thereby lowering computational complexity. The final 1×1 Conv layer merely changes the number of channels, with relatively low computational complexity. The fifth layer is equipped with a 1×1 Conv layer that further reduces the count of channels in the input feature map to 2. The sixth layer is an Avg-pool layer with a kernel size of 3 and a stride of 2, which decreases the height and width of the input feature map from $(Q + 2) \times (1 + 2)$ to $\lfloor (Q + 1)/2 \rfloor \times 1$. The primary role of the fifth and sixth layers is to decrease the input dimensionality for the seventh linear layer, thereby effectively reducing the parameters and computational complexity of the linear layer. Ultimately, the seventh linear layer is responsible for outputting the predicted signal, with an output dimension of $(N + 1) \times M \times 2$.

Algorithm 1 Proposed FL-DRN-NFCE algorithm

Initialization: initialize trainable parameters, $i, j = 0$, raw training data $\mathbf{y}_{t,k}^p, \mathbf{h}'_{t,k}$

Training:

- 1: Input training dataset for all regions
- 2: **while** $j < J$ **do**
- 3: Update α by backpropagation (BP) algorithm to minimize the loss function of the RC
- 4: $j = j + 1$
- 5: **end while**
- 6: Output well-trained RC network

Testing:

- 7: Input testing set
- 8: **do** classification using proposed RC network in Fig. 2
- 9: Output classified dataset

Training:

- 10: Input training dataset for the current region
- 11: **while** $i < I_t$ **do**
- 12: Update θ by BP algorithm to minimize $\mathcal{L}(\theta)$
- 13: $i = i + 1$
- 14: **end while**
- 15: Output well-trained SR-DRN-NFCE network

Testing:

- 16: Input testing set
 - 17: **do** channel estimation using proposed FL-DRN-NFCE network in Fig. 2
 - 18: Output estimated channel
-

4.3 Computational complexity analysis

4.3.1 For the proposed RC network

The computational complexity of the 1st Conv [35] layer is

$$C_{r1} = \mathcal{O}\left((3^2 \cdot 2 \cdot 32) \times (Q \cdot 1)\right) = \mathcal{O}(576Q). \quad (60)$$

Similarly, the computational complexity of the 2rd and 3th Conv layers are

$$C_{r2} = \mathcal{O}\left((3^2 \cdot 32 \cdot 64) \times (Q \cdot 1)\right) = \mathcal{O}(18432Q). \quad (61)$$

and

$$C_{r3} = \mathcal{O}\left((3^2 \cdot 64 \cdot 128) \times (Q \cdot 1)\right) = \mathcal{O}(73728Q). \quad (62)$$

respectively. From Fig. 2, the computational complexity of the 4-th Conv layer is

$$C_{r4} = \mathcal{O}\left((1 \cdot 1 \cdot 128 \cdot 2) \times (Q \cdot 1)\right) = \mathcal{O}(256Q). \quad (63)$$

Under the premise of only considering multiplication operations, the computational complexity of the final linear layer [36] of the proposed RC network is as follows

$$C_{r5} = \mathcal{O}\left((Q \cdot 1 \cdot 2) \times (T \cdot 1 \cdot 1)\right) = \mathcal{O}(2QT). \quad (64)$$

Therefore, the total computational complexity of the proposed RC network is

$$C_r = C_{r1} + C_{r2} + C_{r3} + C_{r4} + C_{r5} = \mathcal{O}(92992Q + 2QT). \quad (65)$$

4.3.2 For the proposed FL-DRN-NFCE network

Based on Fig. 2 and Table 2, the computational complexity of the 1st Conv layer in the proposed FL-DRN-NFCE network is

$$C_{f1} = \mathcal{O}(3^2 \cdot 2 \cdot 32 \times (Q + 2) \cdot (1 + 2)) = \mathcal{O}(1728(Q + 2)). \quad (66)$$

In addition, the calculation method for the complexity of the three residual blocks is similar, as follows

$$\begin{aligned} C_{f2} &= \mathcal{O}((1^2 \cdot 32 \cdot 16 + 3^2 \cdot 16 \cdot 16 + 1^2 \cdot 16 \cdot 64 + 1^2 \cdot 32 \cdot 64) \times (Q + 2) \cdot (1 + 2)) = \mathcal{O}(17664(Q + 2)), \\ C_{f3} &= \mathcal{O}((1^2 \cdot 64 \cdot 32 + 3^2 \cdot 32 \cdot 32 + 1^2 \cdot 32 \cdot 128 + 1^2 \cdot 64 \cdot 128) \times (Q + 2) \cdot (1 + 2)) = \mathcal{O}(70656(Q + 2)), \\ C_{f4} &= \mathcal{O}((1^2 \cdot 128 \cdot 64 + 3^2 \cdot 64 \cdot 64 + 1^2 \cdot 64 \cdot 256 + 1^2 \cdot 128 \cdot 256) \times (Q + 2) \cdot (1 + 2)) \\ &= \mathcal{O}(282624(Q + 2)). \end{aligned} \quad (67)$$

The computational complexity of the Conv layer after three residual blocks is as follows

$$C_{f5} = \mathcal{O}(1^2 \cdot 256 \cdot 2 \times (Q + 2) \cdot (1 + 2)) = \mathcal{O}(1536(Q + 2)). \quad (68)$$

The computational complexity of the linear layer of the proposed FL-DRN-NFCE network is as follows

$$C_{f6} = \mathcal{O}(\lfloor (Q + 1)/2 \rfloor \cdot 1 \cdot 2 \times (N + 1) \cdot M \cdot 2). \quad (69)$$

Therefore, the total computational complexity of the proposed FL-DRN-NFCE network is

$$C_f = C_{f1} + C_{f2} + C_{f3} + C_{f4} + C_{f5} + C_{f6} = \mathcal{O}\left(374208(Q + 2) + 4M(N + 1)(\lfloor (Q + 1)/2 \rfloor)\right). \quad (70)$$

5 Simulation results

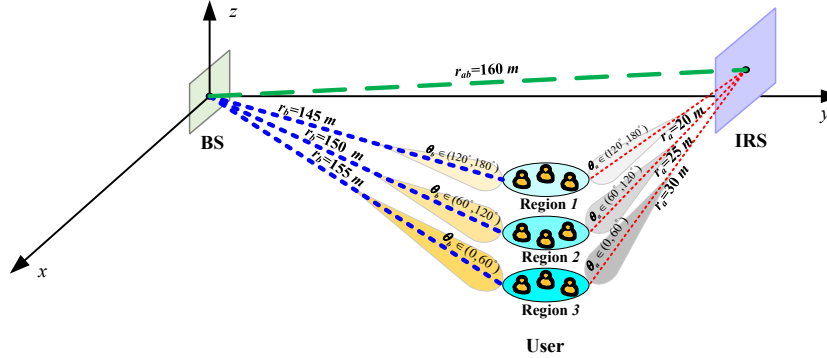


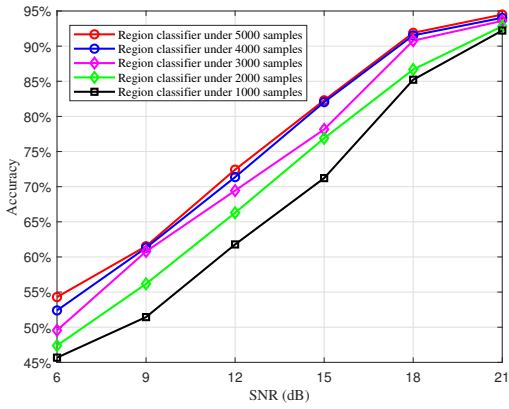
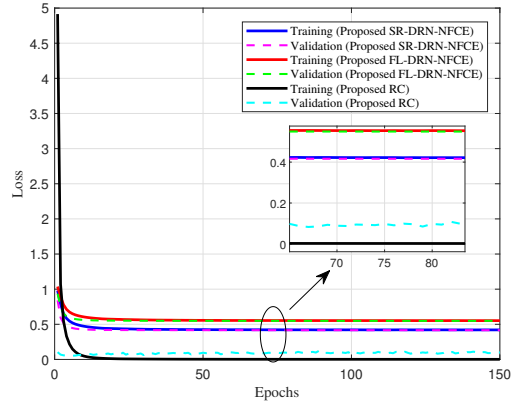
Figure 3 Simulation parameters setup for an IRS-aided MU NF communication.

In this section, the simulation results are given to substantiate the validity of the proposed FL-DRN-NFCE network. Firstly, the configuration of IRS assisted MU NF system is shown in Fig. 3, which consists of three regions with three users in each region. Specifically, M and N are considered to be $M = M_{xb} \times M_{zb} = 3 \times 41 = 123$ and $N = N_{xa} \times N_{za} = 3 \times 41 = 123$, respectively. The azimuth angle and elevation angle of the center of BS's UPA relative to the center of IRS's UPA are $\theta_{ba} = \frac{\pi}{4}$ and $\phi_{ba} = \frac{\pi}{4}$. The other specific parameter configurations are detailed in Table 3. Among them, the azimuths of the $\mathbf{h}_{t,k}$ and $\mathbf{f}_{t,k}$ channels are uniformly distributed in $[0, 2\pi)$ and are equally divided into three parts to correspond to three different user regions in the system. In addition, as depicted in Table 3, the NF distances between users in these three regions and BS and IRS are different. According to [37], r_a and r_{ab} are consistent with the following equation, then IRS-assisted communication operates in the NF region,

$$\frac{r_a \times r_{ab}}{r_a + r_{ab}} < R_{RD} = \frac{2 \times D_{IRS}^2}{\lambda}. \quad (71)$$

Table 3 Simulation parameters setup for the NF scenario.

Parameters	Value
The azimuth angle of $\mathbf{h}_{t,k}$ in three regions	$\theta_b \in \left\{ \left(0, \frac{\pi}{3}\right), \left(\frac{\pi}{3}, \frac{2\pi}{3}\right), \left(\frac{2\pi}{3}, \pi\right) \right\}$
The elevation angle of $\mathbf{h}_{t,k}$ in three regions	$\phi_b \in \left(\frac{\pi}{4}, \frac{\pi}{2}\right)$
Distance between the user in three regions and BS	$r_b = \{145, 150, 155\}$ m
The azimuth angle of $\mathbf{f}_{t,k}$ in three regions	$\theta_a \in \left\{ \left(0, \frac{\pi}{3}\right), \left(\frac{\pi}{3}, \frac{2\pi}{3}\right), \left(\frac{2\pi}{3}, \pi\right) \right\}$
The elevation angle of $\mathbf{f}_{t,k}$ in three regions	$\phi_a \in \left(\frac{\pi}{4}, \frac{\pi}{2}\right)$
Distance between the user in three regions and IRS	$r_a = \{20, 25, 30\}$ m
Distance between BS and IRS	$r_{ab} = r_{ba} = 160$ m
Carrier frequency	$f = 10$ GHz
Wavelength	$\lambda = \frac{c}{f} = \frac{3 \times 10^8}{10 \times 10^9} = 0.03$ m
Element spacing of IRS	$d_{xa} = d_{za} = \frac{\lambda}{2}$
Antenna spacing of BS	$d_{xb} = d_{zb} = \frac{\lambda}{2}$
Width and height of IRS	$L_{xa} = N_{xa} \times d_{xa}$ and $L_{za} = N_{za} \times d_{za}$
Aperture of IRS	$D_{\text{IRS}} = \sqrt{L_{xa}^2 + L_{za}^2}$


Figure 4 The accuracy of the proposed RC network.

Figure 5 The training and the validation loss of the proposed RC, DRN-NFCE, and FL-DRN-NFCE network versus the training epochs.

For comparative analysis, in the FF scenario, the distances between users in the three regions and BS and IRS are set as $r_{b, far} = \{400, 500, 600\}$ m and $r_{a, far} = \{300, 400, 500\}$ m, respectively. Moreover, the \mathbf{G} channel contains $L_{ab} = 15$ NLoS path components, while the NLoS path components of the $\mathbf{h}_{t,k}$ and $\mathbf{f}_{t,k}$ channels in the three regions are $L_b = \{2, 4, 6\}$ and $L_a = \{3, 5, 7\}$, respectively. Specifically, the distance of the NLoS path components in $\mathbf{h}_{t,k}$ is defined to be generated in range of $(R_{min,b}, R_{max,b})$ for three regions, namely $R_{min,b} = \{20, 21, 22\}$ and $R_{max,b} = \{100, 101, 102\}$. Similarly, for $\mathbf{f}_{t,k}$, we have $R_{min,a} = \{15, 20, 25\}$ and $R_{max,a} = \{20, 25, 30\}$. Furthermore, the distance of the NLoS path of \mathbf{G} is generated within the range of $[30, 120]$ and $[25, 100]$. For the proposed FL-DRN-NFCE network, the required pilot overhead is considered to be set to $Q_1 = \frac{M(N+1)}{6} = 2542$, while the traditional LS and MMSE algorithms require a pilot overhead of $Q_2 = M(N+1) = 15252$.

Fig. 4 shows the accuracy of the proposed RC network versus different SNRs. From Fig. 4, it can be observed that as the number of region samples increases, the classification accuracy gradually improves. When the sample size reaches 4000, continuing to increase the sample size does not improve the accuracy significantly. Thus, each user is set to collect 5000 samples as a training set. Moreover, the proposed RC network can reach 95% accuracy in the high SNR range.

As is clearly evident from Fig. 5, the performance of the networks we designed has stabilized and converged in terms of loss on both the training and validation sets after 150 epochs, with the losses falling within acceptable ranges. During the training process, to rapidly reduce the networks' losses and effectively mitigate overfitting, we adopted a LR decay strategy. Specifically, at the early stages of training, we initialized the LR to $1e-3$. This relatively high initial value aided the models in quickly capturing the primary features within the data. Following this, we halved the LR every 15 epochs, progressively decreasing the learning step sizes. The merit of dynamically adjusting the LR in this

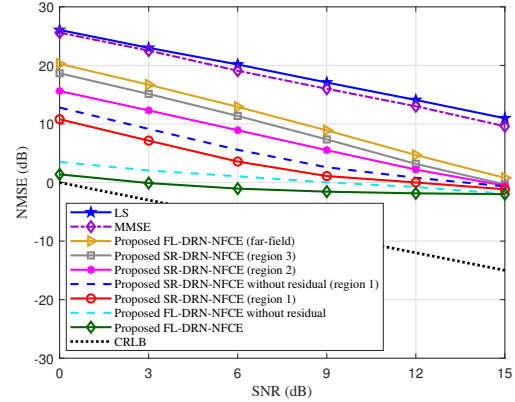
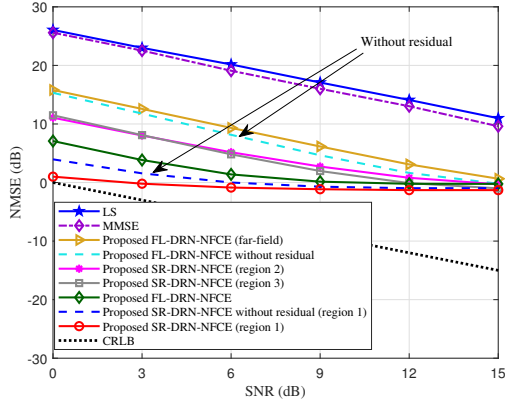


Figure 6 NMSE performance comparison for the region 1. **Figure 7** NMSE performance comparison for the whole region.

fashion is that it not only accelerates the convergence speed of the models but also significantly boosts their ultimate performances, ensuring stability and accuracy in handling complex tasks.

Fig. 6 demonstrates the normalized MSE (NMSE) performance comparison of the proposed SR-DRN-NFCE and FL-DRN-NFCE network versus different SNRs on the testing set from region 1. According to Fig. 6, it can be noticed that the proposed SR-DRN-NFCE network trained only on region 1 achieved the lower MSE on the testing set on region 1. However, the proposed SR-DRN-NFCE network trained on region 2 and region 3 did not work well on region 1.

Fig. 7 describes the NMSE performance comparison of the proposed SR-DRN-NFCE and FL-DRN-NFCE network versus different SNRs on the testing set from the whole region. It can be clearly remarked that the proposed FL-DRN-NFCE network achieved reliable CE in the entire region's test set, which verifies that the training method based on FL can learn different channel characteristics of more users.

From Figs 6 and 7, it can be seen that both the proposed SR-DRN-NFCE and the proposed FL-DRN-NFCE have smaller errors than their corresponding networks without residual connections, which proves the denoising advantage of residual networks. The LS and MMSE schemes require significant pilot overhead to achieve good estimation accuracy, while the two proposed residual methods can achieve better CE performance while reducing pilot overhead by five-sixth.

6 Conclusion

In this paper, channel estimation of IRS-aided NF MU MIMO system has been investigated. The LS estimator, MMSE estimator, and CRLB were derived. Subsequently, in order to reduce pilot overhead and improve CE precision, the SR-DRN-NFCE and FL-DRN-NFCE were proposed. Compared with traditional methods such as LS and MMSE, the proposed FL-DRN-NFCE framework have successfully reduced pilot overhead by five-sixth. Simulation results revealed that the proposed FL-DRN-NFCE framework presented a lower MSE compared to the scheme without residual connection. The accuracy of the proposed RC was approached 95% when the number of user samples was 5000. Lastly, the computational complexity of the proposed RC and FL-DRN-NFCE was delineated. In the whole region, the proposed methods were in an ascending order in term of MSE: FL-DRN-NFCE, SR-DRN-NFCE, MMSE, and LS. In the extremely SNR range, the proposed FL-DRN-NFCE achieves about one-magnitude improvement over SR-DRN-NFCE in term of MSE performance.

Acknowledgements This work was supported in part by the National Natural Science Foundation of China under Grant U22A2002, and by the Hainan Province Science and Technology Special Fund under Grant ZDYF2024GXJS292; in part by the Scientific Research Fund Project of Hainan University under Grant KYQD(ZR)-21008; in part by the Collaborative Innovation Center of Information Technology, Hainan University, under Grant XTCX2022XXC07; in part by the National Key Research and Development Program of China under Grant 2023YFF0612900.

References

- Shu F, Teng Y, Li J Y, et al. Enhanced secrecy rate maximization for directional modulation networks via IRS. *IEEE Trans Commun*, 2021, 69: 8388–8401
- Wang Y, Shu F, Zhuang Z H, et al. Asymptotic performance analysis of large-scale active IRS-aided wireless network. *IEEE Open J Commun Soc*, 2023, 4: 2684–2696

- 3 Yu G H, Chen X M, Shao X D, et al. Low-cost intelligent reflecting surface aided Terahertz multiuser massive MIMO: design and analysis. *Sci. China Inf. Sci*, 2021, 64: 200302
- 4 Hu X L, Wang J W, Zhong C J. Statistical CSI based design for intelligent reflecting surface assisted MISO systems. *Sci. China Inf. Sci*, 2020, 63: 222303
- 5 Tao Q, Zhang S W, Zhong C J, et al. Joint information transmission design for intelligent reflecting surface aided system with discrete phase shifts. *Sci. China Inf. Sci*, 2023, 66: 132303
- 6 Wang X H, Shu F, Shi W P, et al. Beamforming Design for IRS-Aided Decode-and-Forward Relay Wireless Network. *IEEE Trans Green Commun Netw*, 2022, 6: 198–207
- 7 Zheng B X, You C S, Mei W D, et al. A survey on channel estimation and practical passive beamforming design for intelligent reflecting surface aided wireless communications. *IEEE Commun Surv Tutor*, 2022, 24: 1035–1071
- 8 Wang S L, Li Q, Lin J R. One-bit channel estimation for IRS-aided millimeter-wave massive MU-MISO system. *IEEE Trans Signal Process*, 2023, 71: 3592–3606
- 9 Kim I S, Bennis M, Oh J, et al. Bayesian channel estimation for intelligent reflecting surface-aided mmWave massive MIMO systems with semi-passive elements. *IEEE Trans Wireless Commun*, 2023, 22: 9732–9745
- 10 Chen Z J, Zhao M M, Li M, et al. Joint location sensing and channel estimation for IRS-aided mmWave ISAC systems. *IEEE Trans Wireless Commun*, 2024, 23: 11985–12002
- 11 Guan X R, Wu Q Q, Zhang R. Anchor-assisted channel estimation for intelligent reflecting surface aided multiuser communication. *IEEE Trans Wireless Commun*, 2022, 21: 3764–3778
- 12 Zheng B X, Lin S E, Zhang R. Intelligent reflecting surface-aided LEO satellite communication: cooperative passive beamforming and distributed channel estimation. *IEEE J Sel Areas Commun*, 2022, 40: 3057–3070
- 13 Ye M, Zhang H, Wang J B. Channel estimation for intelligent reflecting surface aided wireless communications using conditional GAN. *IEEE Commun Lett*, 2022, 26: 2340–2344
- 14 Ye M, Liang X, Pan C H, et al. GNN-based channel estimation for intelligent reflecting surface aided multiuser systems relying on user locations. *IEEE Wireless Commun Lett*, 2024, 13: 2110–2114
- 15 Shi H Q, Huang Y M, Jin S, et al. Automatic high-performance neural network construction for channel estimation in IRS-aided communications. *IEEE Trans Wireless Commun*, 2024, 23: 10667–10682
- 16 Chu H Y, Pan X, Jiang J, et al. Adaptive and robust channel estimation for IRS-aided millimeter-wave communications. *IEEE Trans Veh Technol*, 2024, 73: 9411–9423
- 17 Wei X H, Dai L L. Channel estimation for extremely large-scale massive MIMO: far-field, near-field, or hybrid-field? *IEEE Commun Lett*, 2022, 26: 177–181
- 18 Cui M Y, Dai L L. Channel estimation for extremely large-scale MIMO: far-field or near-field? *IEEE Trans Commun*, 2022, 70: 2663–2677
- 19 Wang D W, Li X R, He Y X, et al. Intelligent reflecting surface assisted untrusted NOMA transmissions: a secrecy perspective. *Sci. China Inf. Sci*, 2023, 66: 192302
- 20 Pisharody J N, Rajoriya A, Budhiraja R. Near-field channel estimation for XL-MIMO systems using variational Bayesian learning. *IEEE Trans Wireless Commun*, 2024, 23: 10740–10756
- 21 Huang C, Xu J D, Xu Wei, et al. Low-complexity channel estimation for extremely large-scale MIMO in near field. *IEEE Wireless Commun Lett*, 2024, 13: 671–675
- 22 Guo X F, Chen Y B, Wang Y. Compressed channel estimation for near-field XL-MIMO using triple parametric decomposition. *IEEE Trans Veh Technol*, 2023, 72: 15040–15045
- 23 Zhang X Y, Wang Z N, Zhang H Y, et al. Near-Field channel estimation for extremely large-scale array communications: a model-based deep learning approach. *IEEE Commun Lett*, 2023, 27: 1155–1159
- 24 Yang S J, Lyu W T, Hu Z Z, et al. Channel estimation for near-field XL-RIS-aided mmWave hybrid beamforming architectures. *IEEE Trans Veh Technol*, 2023, 72: 11029–11034
- 25 Dai L L, Wei X H. Distributed machine learning based downlink channel estimation for RIS assisted wireless communications. *IEEE Trans Commun*, 2022, 70: 4900–4909
- 26 Liu Y W, Wang Z L, Xu J Q, et al. Near-field communications: a tutorial review. *IEEE Open J Commun Soc*, 2023, 4: 1999–2049
- 27 Storer D, Nehorai A. Passive localization of near-field sources by path following. *IEEE Trans Signal Process*, 1994, 42: 677–680
- 28 Björnson E, Demir Ö T, Sanguinetti L. A primer on near-field beamforming for arrays and reconfigurable intelligent surfaces. In: *Proceedings of 2021 55th Asilomar Conference on Signals, Systems, and Computers*, Pacific Grove, CA, USA, 2021. 105–112
- 29 Biguesh M, Gershman A B. Training-based MIMO channel estimation: a study of estimator tradeoffs and optimal training signals. *IEEE Trans Signal Process*, 2006, 54: 884–893
- 30 Rao X B and Lau V. K. N., Distributed compressive CSIT estimation and feedback for FDD multi-user massive MIMO systems, *IEEE Trans Signal Process*, 2014, 62: 3261–3271
- 31 Liu C, Liu X M, Ng D W K, et al. Deep residual learning for channel estimation in intelligent reflecting surface-assisted multi-user communications. *IEEE Trans Wireless Commun*, 2022, 21: 898–912
- 32 Lu Y, Dai L L. Near-field channel estimation in mixed LoS/NLoS environments for extremely large-scale MIMO systems. *IEEE Trans Commun*, 2023, 71: 3694–3707
- 33 He K M, Zhang X Y, Ren S Q, et al. Deep residual learning for image recognition. In: *Proceedings of 2016 IEEE Conference on Computer Vision and Pattern Recognition (CVPR)*, 2016. 770–778
- 34 Sandler M, Howard A, Zhu M L, et al. MobileNetV2: inverted residuals and linear bottlenecks. In: *Proceedings of 2018 IEEE/CVF Conference on Computer Vision and Pattern Recognition*, 2018. 4510–4520
- 35 Dong P H, Zhang H, Li G Y, et al. Deep CNN-based channel estimation for mmWave massive MIMO systems. *IEEE J Sel Top Signal Process*, 2019, 13: 989–1000
- 36 Liu J J, Hou Q B, Liu Z A, et al. PoolNet+: exploring the potential of pooling for salient object detection. *IEEE Trans Pattern Anal Mach Intell*, 2023, 45: 887–904
- 37 Cui M Y, Wu Z D, Lu Y, et al. Near-field MIMO communications for 6G: fundamentals, challenges, potentials, and future directions. *IEEE Commun Mag*, 2023, 61: 40–46